High-Mobility Ambipolar Magnetotransport in Topological Insulator Bi_2Se_3 Nanoribbons

Gunta Kunakova,[1,2,*] Thilo Bauch,[1] Xavier Palermo,[1] Matteo Salvato,[3] Jana Andzane,[2] Donats Erts,[2] and Floriana Lombardi[1,†]

[1] *Quantum Device Physics Laboratory, Department of Microtechnology and Nanoscience, Chalmers University of Technology, Göteborg SE-41296, Sweden*

[2] *Institute of Chemical Physics, University of Latvia, Raina Blvd. 19, Riga LV-1586, Latvia*

[3] *Dipartimento di Fisica, Università di Roma "Tor Vergata", Roma 00133, Italy*

(Received 30 March 2021; revised 8 June 2021; accepted 12 July 2021; published 23 August 2021)

Nanoribbons of topological insulators (TIs) have been suggested for a variety of applications exploiting the properties of the topologically protected surface Dirac states. In these proposals it is crucial to achieve a high tunability of the Fermi energy, through the Dirac point while preserving a high mobility of the involved carriers. Tunable transport in TI nanoribbons has been achieved by chemical doping of the materials so to reduce the bulk carriers' concentration, however at the expense of the mobility of the surface Dirac electrons, which is substantially reduced. Here we study bare Bi_2Se_3 nanoribbons transferred on a variety of oxide substrates and demonstrate that the use of a large relative permittivity $SrTiO_3$ substrate enables the Fermi energy to be tuned through the Dirac point and an ambipolar field effect to be obtained. Through magnetotransport and Hall conductance measurements, performed on single Bi_2Se_3 nanoribbons, we demonstrate that electron and hole carriers are exclusively high-mobility Dirac electrons, without any bulk contribution. The use of $SrTiO_3$ allows therefore an easy field effect gating in TI nanostructures providing an ideal platform to take advantage of the properties of topological surface states.

DOI: 10.1103/PhysRevApplied.16.024038

I. INTRODUCTION

Topological-insulator (TI) nanoribbons are considered promising candidates for a variety of applications, which can take advantage from the high surface-to-volume ratio and the reduced number of electronic transport modes. For example, improved thermoelectric performance in very thin TI nanoribbons can be foreseen because of the topological surface states and the gap opening at the Dirac point and the reduction of phonon thermal conductivity due to scattering from the surfaces [1,2]. At the same time the low number of transport modes have been shown to be advantageous when realizing Josephson junctions with TI nanoribbons [3–5] for the exploitation of Majorana fermions in topological quantum computation [6,7].

To take advantage of the peculiar properties of TI nanoribbons it is imperative to reduce the contribution of the bulk carriers as well as to be able to tune the Fermi energy across the Dirac point [8–12]. Up to now doping has been successfully used for nanoribbons to eliminate the bulk contribution, however at the expense of the mobility of the surface Dirac electrons, which is heavily reduced [10]. High mobility is instrumental for applications, so doping does not appear a viable strategy to take full advantage of the Dirac electron physics. Another critical issue, affecting TI nanoribbon devices, is the unavoidable presence of an oxide layer around the external surface [13,14], which may lead to the formation of an extra two-dimensional (2D) gas once they are transferred on oxide dielectric substrates. It is well established, for example, that in high-k–SiO_2 interfaces, oxygen displacement at the interface is responsible for the formation of interface dipoles with an orientation depending on the density difference of oxygen atoms at the interface [15–17]. The sign of the dipole can determine the formation of a depletion or an accumulation layer at the interface between the two oxides. We have recently demonstrated that in the case for Bi_2Se_3 nanoribbons transferred on a SiO_2/Si substrate a 2D accumulation layer, with a high carrier density up to 2×10^{13} cm^{-2}, is formed at the interface with the SiO_2 [18,19]. This makes it difficult to tune the Fermi level close to the Dirac point due to the relatively low dielectric

*gunta.kunakova@lu.lv

†floriana.lombardi@chalmers.se

constant of the substrate. It is therefore crucial to explore the behavior of TI nanoribbons once transferred on substrates with different properties to fully access the Dirac point physics of TI nanoscale devices.

In this paper, we implement Bi_2Se_3 nanoribbons on various oxide substrates and demonstrate that the formation of an accumulation layer is a general feature characterizing the interface with Bi_2Se_3. In particular we show that the use of $SrTiO_3$ (STO) enables us (a) to completely deplete the interface accumulation layer by back gating through the substrate, (b) to tune the Fermi surface through the Dirac point, and finally (c) to obtain an ambipolar field effect; here the electrons and holes exclusively belong to the Dirac bands (without any bulk contribution) from the top and bottom surface of the nanoribbon. The combination of these three findings can bring forward the implementation of TI nanoribbons in devices, which take advantage of the unique properties of the topological surface states.

II. EXPERIMENTAL RESULTS AND DISCUSSION

Charge transport in topological-insulator Bi_2Se_3 nanoribbons transferred on SiO_2/Si substrates has previously been found to be affected by a strong downward band bending at the interface with the substrate, which implies the formation of a trivial 2DEG accumulation layer at the interface between the nanoribbon's bottom surface and the substrate. See Fig. S1 within the Supplemental Material for a schematic of the band-bending diagram [20], and in Refs. [18,19]. To evaluate the effect that different substrates might have on the nanoribbon band structure, we compare the carrier densities of nanoribbons with similar thicknesses once they are transferred on the substrates under study $-SiO_2/Si$ i.e. Si substrates covered by 300 nm of SiO_2; as delivered STO (100) with mixed termination surface of SrO and TiO_2 oxides; TiO_2-terminated STO (100); and sapphire. The carrier density of individual nanoribbons is measured via Hall effect. A SEM image of one of the nanoribbon Hall bar devices on a STO substrate is shown in Fig. 1(a). The values of the carrier density n_{3D} are calculated from the Hall resistance as

$$\frac{1}{n_{3D}e} = t\frac{dR_{xy}}{dB} \times g, \tag{1}$$

where e is the elementary charge; t is the thickness of the nanoribbon, and g is a correction factor of the measured Hall voltage due to the nonideal Hall bar geometry [21]. We numerically calculate the correction factor using COMSOL for our typical Hall bar geometries and contact resistances, obtaining $g \approx 6$. See Supplemental Material for the simulation of the Hall voltage correction factor g, and for details of all the measured nanoribbons listed in Table S1 [20]. The carrier density values for nanoribbons with thicknesses in the range 7–24 nm, for the various

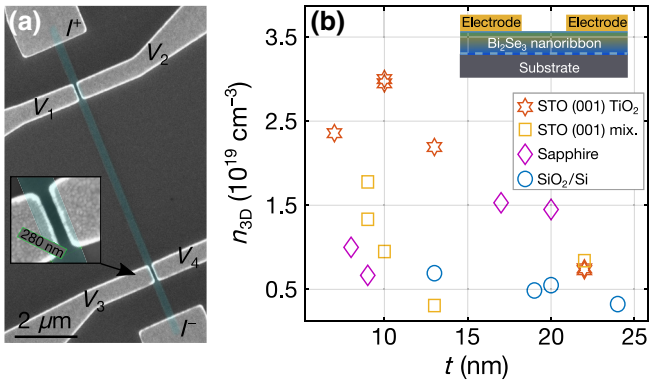

FIG. 1. (a) SEM image of the Bi_2Se_3 nanoribbon with electrodes for Hall-effect measurement. (b) Hall carrier density n_{3D} for Bi_2Se_3 nanoribbons within the thickness range of 7–24 nm and transferred on four different substrates. The inset shows a cross-section schematic of the nanoribbon device: the light blue dashed line highlights the interface between the nanoribbon bottom surface and the substrate where the accumulation layer is located.

substrates are plotted in Fig. 1(b). The n_{3D} of thin nanoribbons on SiO_2/Si is approximately 5×10^{18} cm^{-3} and it increases up to 3×10^{19} cm^{-3} for TiO_2-terminated STO substrates.

The extracted values of n_{3D} are the largest for TiO_2-terminated substrates in line with a higher value of the electron affinity EA of TiO_2 [22]. The lowest values for n_{3D} are instead found for SiO_2/Si substrates in agreement with the lowest EA value among the substrates investigated in this work [22]. While the data of Fig. 1(b) suggest that SiO_2/Si is the best substrate among the ones of this study, its low dielectric constant ($\varepsilon_{SiO_2} \approx 3.5$ [23]) gives a poor tunability of the nanoribbon carrier density by using back gate. With STO substrates, instead, because of the extremely high dielectric constant ($\varepsilon_{STO,65K} \approx 1000$ and $\varepsilon_{STO,1K} \approx 20\,000$) [24], the tunability of the device is highly increased. STO (001) substrates with dominant TiO_2-terminated surface would in principle be a better option compared to the nontreated STO, due to the atomically flat surface steps [25,26] and uniformity of the oxide surface in contact with the nanoribbon. However, due to the high electron affinity of TiO_2, the initial 2D carrier density formed at the interface with the Bi_2Se_3 nanoribbon is too high to be fully depleted by the back gate, see Fig. S2 within the Supplemental Material [20]. Indeed, as we show below an ambipolar transport can only be achieved in nanoribbon devices fabricated on STO (001) with mixed SrO and TiO_2 terminated surface. For these devices, gate efficiency varies depending on the nanoribbons' thickness and on the substrate-nanoribbon interface, which is affected by the substrate's surface termination. The ambipolar transport can only be achieved in very thin nanoribbons (in our case 9 nm thick) as also reported in the literature [9,10,12].

The electron affinity of STO (001) with a mixed SrO and TiO_2 is expected to be smaller than the affinity of STO-TiO_2 ($EA_{STO,TiO_2term.} = 3.57$ eV [27]) and comparable to value of SiO_2 on Si substrate as $EA_{STO,\,SrO\,term.} = 1.27$ eV [27] and $EA_{SrO} = 0.64$ eV [28] are about 3 and 5 times smaller, respectively, as compare to EA_{STO,TiO_2term}.

Figure 2(a) shows the longitudinal resistance R_{xx} as a function of the applied back-gate voltage V_g for the Bi_2Se_3 nanoribbon device B51-10 fabricated on a STO substrate with mixed termination. The $R_{xx}(V_g)$ displays a hysteretic characteristic. This behavior is known to be present in devices fabricated on STO substrates and has been attributed to the formation of ferroelectriclike surface dipoles in the STO [29]. The hysteresis also depends on the sweep history: the initial resistance of approximately equal to 20 kΩ at $V_g = 0$ V is increased to nearly 3 times larger value after a first scan with the gate voltage applied as follows: 0 to −40, −40 to 40 and 40 to 0 V [red arrows in Fig. 2(a)]. However, the value of the resistance at the end of the first scan can be switched back to its initial value by performing a second scan, by using gate voltages applied with an reversed sequence: 0 to 40; 40 to −40 and −40 to 0 V [Fig. 2(a), gray arrows]. It is useful to note, that the hysteresis and the sweep history is less pronounced, if the gate-sweeping range is limited to only negative (positive) values.

The back-gate dependence of the Hall carrier density extracted using Eq. (1) is plotted in Fig. 2(a). At $V_g = 0$ V, the slope of $R_{xy}(B)$ is negative [Fig. 2(c), green stars] indicating electrons as the majority charge carriers. By increasing the back-gate voltage for negative values at about $V_g = -17$ V, the $R_{xy}(B)$ slope becomes positive indicating the dominating carriers in the nanoribbon have switched from *n* type to *p* type. This change occurs in the gate-voltage range between −13 and −17 V, which coincides with the voltage range where a kink in the $R_{xx}(V_g)$ dependence is observed [Fig. 2(a), 0 to −40 V scan]. An ambipolar behavior has been previously reported for large flakes and thin films of Bi_2Se_3 and other three-dimensional (3D) TIs [8,10,30,31]; it clearly indicates a Fermi-level tuning across the Dirac point.

The nanoribbon under consideration has a thickness of 9 nm close to the thickness of 6–7 nm (considering the oxide shell formed around) previously found to be optimal for topological surface-state-dominated charge transport [32]. However, in our case the total carrier density at $V_g = 0$ V also includes the carriers from the accumulation layer. To further distinguish the contribution of carriers coming from different bands, we analyze the $R_{xy}(B)$ dependences measured up to 13 T with a two-band model [33]. The black dashed line of the linear fit of the 0–2 T region [Fig. 2(c)] clearly highlights deviation from the linearity at higher magnetic fields. The upward bending for the $V_g = 0$ V

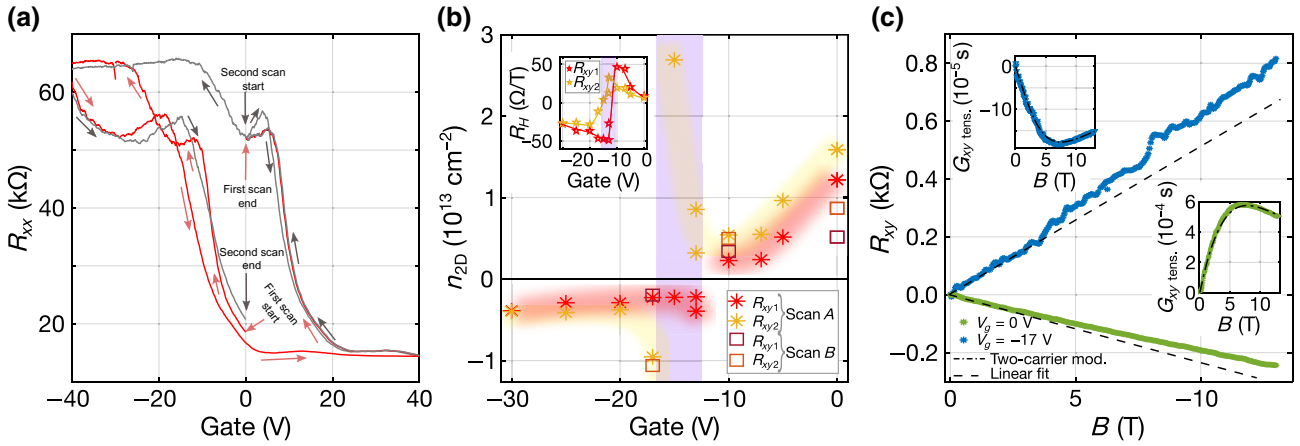

FIG. 2. (a) R_{xx} as a function of back-gate voltage V_g. The red and gray curves represent two different scans and the arrows indicate sweep direction of V_g. The first $R_{xx}(V_g)$ scan is measured with V_g applied as follows: 0 to −40; −40 to 40; 40 to 0 V (red arrows), while the second curve corresponds to the opposite scanning direction 0 to 40; 40 to −40; −40 to 0 V (gray arrows). (b) Hall carrier density n_{2D} as a function of back-gate voltage. The carrier density values shown here are calculated from the linear fits of the antisymmetrized $R_{xy}(B)$ for B in the range −2 to 2 T. The positive sign of n_{2D} indicates electronlike majority carrier concentrations. The inset shows the Hall coefficient as a function of the gate voltage. In both graphs the violet shaded region addresses a mixed region of *n*- and *p*-type carriers. The increase of n_{2D} in the main graph, by going to negative V_g is only "apparent": it is a consequence of the R_H changing sign (see inset), which gives an unrealistically low slope and as a consequence higher value of n_{2D}. The values of n_{2D} in the shaded violet regions therefore do not correspond to effective carriers. R_{xy1} and R_{xy2} are measured using different Hall contacts of the same nanoribbon device, and scan *A* and scan *B* represent two subsequent sweeps. (c) Antisymmetrized $R_{xy}(B)$ in the range of B between −13 to 13 T at back-gate voltage $V_g = 0$ V and $V_g = -17$ V. The black dashed lines are the linear fit in the range of 0 to 2 T. The inset shows the $G_{xy}(B)$ dependences with the fit of the two-carrier model, Eq. (2), (dot dashed line). All the data refer to nanoribbon B51-10.

curve at high magnetic field accounts for the contribution of another band with electron carriers with different mobility; indeed the slope at 10–13 T yields a higher carrier density of 5.75×10^{12} cm^{-2} (as compare to 5.0×10^{12} cm^{-2} calculated from the 0–2 T region). The situation for $R_{xy}(B)$ at $V_g = -17$ V is instead the opposite: we get a reduced value of $n_{2D} = 1.72 \times 10^{12}$ cm^{-2} when considering the slope in the 10–13 T region (1.97×10^{12} cm^{-2} from the slope to 0–2 T). Here the majority of charge carriers (at $V_g = -17$ V) are holes, and the decreased Hall carrier density at higher magnetic field indicates the presence of a small fraction of carriers with opposite sign (in this case electrons). In the two-carrier model, the conductance tensor G_{xy} is written as [33]

$$G_{xy}(B) = eB\left(\frac{n_1{\mu_1}^2}{1+\mu_1{}^2B^2} + \frac{n_2{\mu_2}^2}{1+\mu_2{}^2B^2}\right), \qquad (2)$$

where n_1, n_2 and μ_1, μ_2 are the carrier densities and the mobilities of the two bands. Here we consider that one band is represented by the Dirac electrons at the top surface and the other band includes both the 2D accumulation layer at the interface with the substrate and the Dirac electrons at the bottom surface of the nanoribbon. We instead neglect the carrier band coming from the bulk since in agreement with our previous work where we demonstrate that nanoribbons below 30 nm in thickness are bulk free [18]. The conductance tensor G_{xy} is calculated from the longitudinal and transverse resistances R_{xx} and R_{xy} as

$$G_{xy} = -\frac{R'_{xy}}{{R'_{xy}}^2 + {R'_{xx}}^2}. \qquad (3)$$

Here $R'_{xy} = R_{xy}g$ is the corrected Hall resistance considering the geometry of a narrow Hall bar and $R'_{xx} = R_{xx}w/L$ is the sheet resistance; w and L are the width and length of the nanoribbon, respectively. The $G_{xy}(B)$ dependences are shown in the insets of Fig. 2(c). The dot-dashed lines represent the fit of the data at different gate voltages by using Eq. (2). Table I summarizes the resulting parameters of the fitting procedure.

By using the two-carrier model the carrier densities we extract at the initial state with $V_g = 0$ V are $n_1 = 1.49 \times 10^{11}$ cm^{-2}; $n_2 = 5.55 \times 10^{12}$ cm^{-2} (Table I). From our previous studies [18], the highest density n_2 accounts for the sum of the 2DEG at the nanoribbon-substrate interface and of the carriers from topological surface states at the nanoribbon bottom surface. In this case the minority carrier densities $n_1 = 1.49 \times 10^{11}$ cm^{-2} are representing the topological surface states at the nanoribbon top surface. The Fermi level calculated from the Dirac point at the top surface can be estimated from the relation $E_{(F,1)} = \hbar k_F v_F$, where $k_F = \sqrt{4\pi n_1}$ is the Fermi wave vector, v_F the Fermi velocity of 5×10^5 m/s [34] and $\hbar$ the reduced Planck constant. We get a value within the range of approximately equal to 42–48 meV (considering the confidence interval of our fitting procedure). Once the gate voltage is applied, the Fermi level E_F is tuned through the Dirac point and the nanoribbon enters a regime of majority p-type conduction at negative $V_g = -17$ V. At this point the initial majority electron carriers mostly coming from the trivial 2DEG formed at the interface with the substrate are depleted, becoming therefore the minority carriers.

The carrier density values extracted from the two-carrier analysis at an intermediate value of $V_g = -10$ V (Table I) show the opposite situation as compared to the initial state at $V_g = 0$ V [see $R_{xy}(B)$, $V_g = -10$ V data in Fig. S3 within the Supplemental Material [20]], where the high field carrier density is instead higher as compared to the one extracted from the low magnetic field region

TABLE I. Fitted parameters of the two-band model[a]. $E_{F,1}$ and $E_{F,2}$ are the Fermi energy measured from the Dirac point for the top surface (TS) and bottom surface (BS/Accumulation layer), respectively.

V_g(V)	n_1, TS (10^{11} cm^{-2})	μ_1 (cm^2/Vs)	E_{F1} (meV)	n_2, BS/AL (10^{12} cm^{-2})	μ_2 (cm^2/Vs)	E_{F2} (meV)	n_{2D} (10^{12} cm^{-2})	μ_{Hall} (cm^2/Vs)
B51-10								
0	1.49	4626	45	5.55	1232	–	5.75	1320
	1.31 – 1.69	4394–4858	42–48	5.50 – 5.55	1224–1238			
−10	−1.06	3100	−38	2.31	1100	176	2.64	1048
	−1.25– – 0.87	2569–3632	−41– −33	2.29 – 2.32	1082–1118	175–177		
−17	−16.9	1400	−150	0.069	2700	30	−1.72	1510
	−19.1– – 15.6	1340–1462	−156– −146	0.046 – 0.080	2372–2884	25–33		
B51-9/1								
0	26.2	1900	188	6.36	1095	–	9.51	1920
	25.0 – 27.5	1895–1905	183–192	6.26 – 6.47	1087–1104			
−40	−2.43	1080	−57	1.43	1560	139	1.40	1955
	−2.75– −1.99	1075–1085	−61– −52	1.40 – 1.47	1535–1595	137–141		

[a] Range of the values shown below each of the parameter indicate confidence bounds of the two-carrier model fit; positive sign is for electrons, while negative is for holes.

(3.38×10^{12} and 2.64×10^{12} cm^{-2} from the slopes of 0–2.5 T and 10–13 T magnetic field regions, respectively), indicating that the majority of carriers are electrons, but now there exists also a small fraction of p-type carriers. Decreasing the back-gate voltage even further ($V_g = -17$ V) we obtain for n_2 a value 6.87×10^{10} cm^{-2}. The value of carrier density n_2 decreases steeply by changing the back gate voltage, from 5.55×10^{12} ($V_g = 0$ V) to 6.87×10^{10} ($V_g = -17$ V), with an intermediate value of 2.31×10^{12} cm^{-2} ($V_g = -10$ V), see Fig. S4 within the Supplemental Material [20]. This effective tuning of carriers by the back-gate voltage can be expected, if these carriers originate from the nanoribbon bottom interface.

The estimated values obtained from the two-carrier analysis for $V_g = -17$ V data give an $E_{F,1}$ at the top surface of -150 meV where holes are majority carriers. Indeed for this extremely thin nanoribbon one expects that the bulk band gap is strongly enhanced compared to the bulk crystals [35]. Therefore, we expect that the chemical potential at the top surface $E_{F,1}$ lies within the bulk band gap with Dirac holes as the majority carriers. The schematic band-bending diagrams for $V_g = 0$ V and -17 V are shown in Fig. 3(a) by taking into account the estimated carrier densities with the corresponding values of the E_F.

Similar analysis is performed for an additional nanoribbon B51-9/1, $t = 10$ nm, on the same substrate, but with a slightly higher initial carrier density and thickness, see Table I and Fig. S3 within the Supplemental Material [20]. Carriers of both populations from the top and the bottom surfaces are effectively depleted with the applied negative back-gate voltage $V_g = -40$ V, and the Fermi level $E_{F,1}$ of the B51-9/1 nanoribbon top surface is tuned below the Dirac point, implying the p-type conduction. This behavior is comparable with the one measured for the sample B51-10, at $V_g = -10$ V (Table I). The carrier density of the nanoribbon bottom surface and interface accumulation layer n_2 remains instead n type. This can be understood taking into account the following: (1) nonuniform nanoribbon-substrate interface in the case of STO, mixed termination substrate. It affects formation of the accumulation layer, and in places where patches of TiO_2-terminated oxide dominates, the carrier density will be higher. Initially low carrier density is key for an effective electrostatic gating. (2) Thickness of the nanoribbon. In order to fully suppress the n-type conduction, the nanoribbon thickness should be much smaller than the charge depletion length. For $(Bi_xSb_{1-x})_2Te_3$ it is around 11 nm, and a full depletion to p-type is realized only in 5-nm thin nanoplates [9].

Figure 3(b) shows the temperature dependence of the R_{xx} at different negative back-gate voltages. We initially observe at $V_g = 0$ V that the $R_{xx}(T)$ [Fig. 3(b)] has a metallic behavior. This is what we expect for a transport dominated by the high carrier-density 2DEG at the interface with the substrate. This behavior drastically changes by applying a negative V_g: once the accumulation layer is depleted the nanoribbon enters a regime where the transport is determined by Dirac electrons and thermally excited carriers in the conduction band [see Fig. 3(a) right panel]. These last give the typical semiconductorlike behavior of the longitudinal resistance [see yellow and blue curve in Fig. 3(b)]. However, we cannot completely rule out the effect of a temperature-dependent relative dielectric constant of the STO substrate on the increase of R_{xx} at a finite gate voltage with decreasing temperature [36]. At $V_g = -10$ V we see that below 10 K the thermally excited

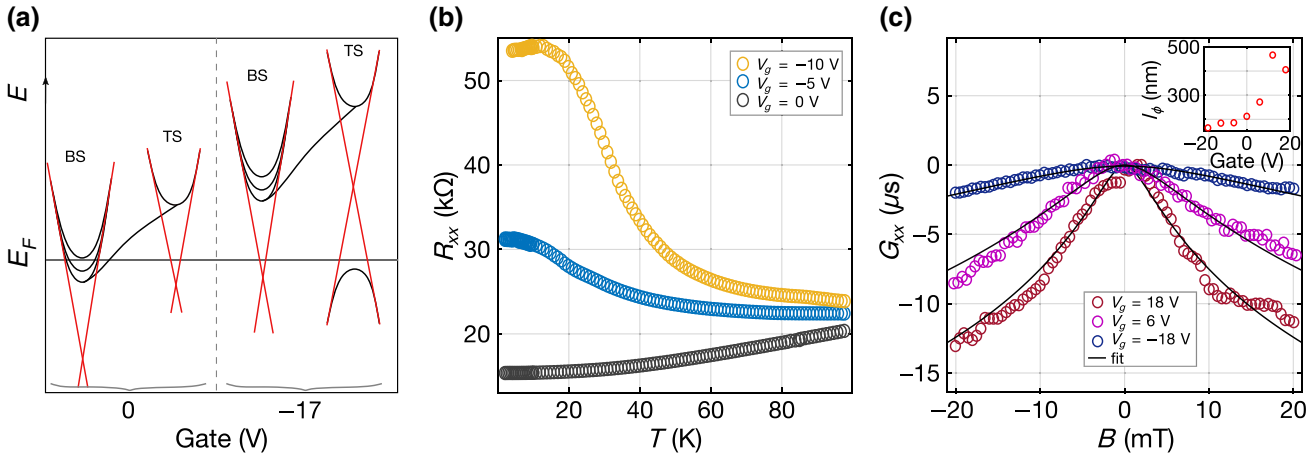

FIG. 3. (a) Schematic representation of the band-bending diagram of a 9-nm-thick Bi_2Se_3 nanoribbon at $V_g = 0; -17$ V, constructed considering the carrier densities determined from the two-carrier model Eq. (2). BS and TS indicate the bottom (in contact with the substrate) and top surfaces, respectively. (b) R_{xx} as a function of temperature for different applied back-gate voltages, nanoribbon B51-10. (c) Excess conductance $\Delta G_{xx}(B) = G_{xx}(B) - G_{xx}(B = 0)$ as a function of magnetic field. The black solid curves are the fits using Eq. (4). The inset shows the phase coherence length extracted from the fitting of $\Delta G_{xx}(B)$ as a function of back-gate voltage.

carriers in the conduction band are frozen out and the Dirac electrons start to dominate the transport giving a metalliclike $R_{xx}(T)$ dependence at low temperature.

The applied back gate also affects the weak antilocalization (WAL) dip, which appears in the conductance versus the external magnetic field and is due to spin-orbit coupling in Bi_2Se_3 [Fig. 3(c)]. We observe that the width of the peak, which is a measure of the phase coherence length l_Φ (and of the number of contributing 2D conduction channels α) increases by applying a negative gate voltage indicating that the phase coherence is dramatically reduced. l_Φ can be estimated using the Hikami-Larkin-Nagaoka (HLN) equation [37], where the excess conductance for a 2D system is given by

$$\Delta G_{xx} = -\alpha \frac{e^2}{2\pi^2 \hbar} \left[ln\left(\frac{\hbar}{4el_\phi^2 B}\right) - \Psi\left(\frac{1}{2} + \frac{\hbar}{4el_\phi^2 B}\right)\right], \tag{4}$$

here $\hbar$ is the reduced Planck constant and Ψ the digamma function. The inset of Fig. 3(c) shows the l_Φ values as a function of the gate voltage V_g. We observe that l_Φ decreases for negative V_g where more p-type carriers contribute to the charge transport. This is in line with the reduced mobility of Dirac holes compared to the one of electrons [38] leading to shorter phase coherence time. In Eq. (4), the parameter α is in the range 0.7–0.85 for negative V_g. This indicates that more than one coherent 2D channel is contributing the charge transport, in agreement with the high field magnetotransport $R_{xy}(B)$ data analysis and a band diagram where Dirac holes at the top surface and Dirac electrons at the bottom surface (at the interface with the substrate) contribute to the transport [see Fig. 3(a)].

To conclude we show that in bare Bi_2Se_3 nanoribbons transferred on the STO substrate the application of a back gate is able to tune the carrier density through the Dirac point, when only Dirac electrons and holes contribute to the transport. In our nanoribbons, the high mobility of the Dirac carriers remains intact, which is of great relevance for applications taking advantage of the topological surface state physics.

III. METHODS

Nanoribbons of Bi_2Se_3 are grown via catalyst-free solid physical vapor deposition method as reported elsewhere [39]. The nanoribbons, obtained on a glass substrate, are free standing and for the measurements of charge transport are transferred to prepatterned substrates of (a) Si substrates covered by 300 nm of SiO_2; (b) as delivered (100) $SrTiO_3$; (c) TiO_2-terminated (100) $SrTiO_3$ (TiO_2-STO) and (d) sapphire, by contact transfer. The TiO_2-terminated substrates are prepared by etching in buffered hydrofluoric acid (BHF) solution (30 s) and annealing at O_2 atmosphere, 950 °C (3 h). Thickness of the STO substrates is 500 μm. To define the electrical contact of individual Bi_2Se_3 nanoribbons, we use electron-beam-lithography processing, followed by Ar^+ etching to remove the native oxide from the Bi_2Se_3 nanoribbons [18,39] and the evaporation of a 3-nm Pt layer and 80-nm Au layer. All the transport measurements are done in a Quantum Design Physical Property Measurement System (PPMS), with a base temperature of 2 K.

We routinely achieve well-aligned electrodes so measurements of the Hall effect are possible even for 200-nm-wide nanoribbons. The Hall resistance R_{xy} is measured using the electrode pairs V_1–V_2 or V_3–V_4 to record the resistances R_{xy1} and R_{xy2}, respectively, under a constant flow of current between the probes $I^+ - I^-$. The external magnetic field is applied perpendicularly to the substrate surface. The longitudinal resistance R_{xx} is recorded in four-probe electrode configuration using the electrode pairs (V_1–V_3 or V_2–V_4).

ACKNOWLEDGMENTS

This work is supported by the European Union's Horizon 2020 research and innovation program, Grant Agreement No. 766714/HiTIMe, by the European Union's project NANOCOHYBRI (Cost Action CA 16218) and Latvian Council of Science, Project No. lzp-2020/2-0343. Authors would like to thank "Vinnova competence center at the Chalmers University of Technology 2D-TECH", and A. Kalaboukhov for preparing TiO_2 – terminated STO (001) substrates.

[1] P. Ghaemi, Roger S. K. Mong, and J. E. Moore, In-Plane Transport and Enhanced Thermoelectric Performance in Thin Films of the Topological Insulators Bi_2Te_3 and Bi_2Se_3, Phys. Rev. Lett. **105**, 166603 (2010).

[2] T.-C. Hsiung, C.-Y. Mou, T.-K. Lee, and Y.-Y. Chen, Surface-dominated transport and enhanced thermoelectric figure of merit in topological insulator $Bi_{1.5}Sb_{0.5}Te_{1.7}Se_{1.3}$, Nanoscale **7**, 518 (2015).

[3] G. Kunakova, T. Bauch, E. Trabaldo, J. Andzane, D. Erts, and F. Lombardi, High transparency Bi_2Se_3 topological insulator nanoribbon josephson junctions with low resistive noise properties, Appl. Phys. Lett. **115**, 172601 (2019).

[4] J. Hajer, M. Kessel, C. Brüne, M. P. Stehno, H. Buhmann, and L. W. Molenkamp, Proximity-induced superconductivity in CdTe - HgTe Core - shell nanowires, Nano Lett. **19**, 4078 (2019).

[5] G. Kunakova, A. P. Surendran, D. Montemurro, M. Salvato, D. Golubev, J. Andzane, D. Erts, T. Bauch, and F. Lombardi, Topological insulator nanoribbon josephson junctions: Evidence for size effect in transport properties, J. Appl. Phys. **128**, 194304 (2020).

[6] L. Fu and C. L. Kane, Superconducting Proximity Effect and Majorana Fermions at the Surface of a Topological Insulator, Phys. Rev. Lett. **100**, 096407 (2008).

[7] J. Manousakis, A. Altland, D. Bagrets, R. Egger, and Y. Ando, Majorana qubits in a topological insulator nanoribbon architecture, Phys. Rev. B - Condens. Matter Mater. Phys. **95**, 165424 (2017).

[8] H. Steinberg, D. R. Gardner, Y. S. Lee, and P. Jarillo- Herrero, Surface state transport and ambipolar electric field effect in Bi_2Se_3 nanodevices, Nano Lett. **10**, 5032 (2010).

[9] D. Kong, Y. Chen, J. J. Cha, Q. Zhang, J. G. Analytis, K. Lai, Z. Liu, S. S. Hong, K. J. Koski, S. K. Mo, Z. Hussain, I. R. Fisher, Z.-X. Shen, and Y. Cui, Ambipolar field effect in the ternary topological insulator $(Bi_xSb_{1-x})_2Te_3$ by composition tuning, Nat. Nanotechnol. **6**, 705 (2011).

[10] S. S. Hong, J. J. Cha, D. Kong, and Y. Cui, Ultra-low carrier concentration and surface-dominant transport in antimony-doped Bi_2Se_3 topological insulator nanoribbons, Nat. Commun. **3**, 757 (2012).

[11] L. A. Jauregui, M. T. Pettes, L. P. Rokhinson, L. Shi, and Y. P. Chen, Gate tunable relativistic mass and Berry's phase in topological insulator nanoribbon field effect devices, Sci. Rep. **5**, 8452 (2015).

[12] J. Lee, J. Park, J. Lee, J. S. Kim, and H. Lee, Gate-tuned differentiation of surface-conducting states in $Bi_{1.5}Sb_{0.5}Te_{1.7}Se_{1.3}$ topological-insulator thin crystals, Phys. Rev. B - Condens. Matter Mater. Phys. **86**, 245321 (2012).

[13] D. Kong, J. J. Cha, K. Lai, H. Peng, J. G. Analytis, S. Meister, Y. Chen, H. J. Zhang, I. R. Fisher, Z. X. Shen, and Y. Cui, Rapid surface oxidation as a source of surface degradation factor for Bi_2Se_3, ACS Nano **5**, 4698 (2011).

[14] W. Ning, H. Du, F. Kong, J. Yang, Y. Han, M. Tian, and Y. Zhang, One-dimensional weak antilocalization in single-crystal Bi_2Te_3 nanowires, Sci. Rep. **3**, 1564 (2013).

[15] K. Kita and A. Toriumi, Origin of electric dipoles formed at high-k/SiO_2 interface, Appl. Phys. Lett. **94**, 92 (2009).

[16] K. Han, X. Wang, H. Yang, and W. Wang, Electric dipole formation at high-k dielectric/SiO_2 interface, J. Semicond. **36**, 2014 (2015).

[17] K. Iwamoto, Y. Kamimuta, A. Ogawa, Y. Watanabe, S. Migita, W. Mizubayashi, Y. Morita, M. Takahashi, H. Ota, T. Nabatame, and A. Toriumi, Experimental evidence for the flatband voltage shift of high-k metal-oxide-semiconductor devices due to the dipole formation at the high-k SiO_2 interface, Appl. Phys. Lett. **92**, 132907 (2008).

[18] G. Kunakova, L. Galletti, S. Charpentier, J. Andzane, D. Erts, F. Léonard, C. D. Spataru, T. Bauch, and F. Lombardi, Bulk-free topological insulator Bi_2Se_3 nanoribbons with magnetotransport signatures of dirac surface states, Nanoscale **10**, 19595 (2018).

[19] G. Kunakova, R. Meija, J. Andzane, U. Malinovskis, G. Petersons, M. Baitimirova, M. Bechelany, T. Bauch, F. Lombardi, and D. Erts, Surface structure promoted high-yield growth and magnetotransport properties of Bi_2Se_3 nanoribbons, Sci. Rep. **9**, 11328 (2019).

[20] See Supplemental Material at http://link.aps.org/supplemental/10.1103/PhysRevApplied.16.024038 for additional figures and simulation of the Hall voltage correction factor.

[21] L. Barbut, F. Jazaeri, D. Bouvet, and J. M. Sallese, Mobility measurement in nanowires based on magnetic field-induced current splitting method in H-shape devices, IEEE Trans. Electron Devices **61**, 2486 (2014).

[22] Electron affinities (EA) of the substrates: $EA_{SiO_2} = 0.95$ eV [23]; $EA_{STO,\,SrO\,term.} = 1.27$ eV [27]; $EA_{SrO} = 0.64$ eV [28]; $EA_{Al_2O_3} = 1.25$ eV [23]; $EA_{STO,TiO_2\,term.} = 3.57$ eV [27]; $EA_{TiO_2} = 4$ eV [40].

[23] R. G. Southwick, A. Sup, A. Jain, and W. B. Knowlton, An interactive simulation tool for complex multilayer dielectric devices, IEEE Trans. Device Mater. Reliability **11**, 236 (2011).

[24] A. Verma, S. Raghavan, S. Stemmer, and D. Jena, Ferroelectric transition in compressively strained $SrTiO_3$ thin films, Appl. Phys. Lett. **107**, 192908 (2015).

[25] D. Kobayashi, H. Kumigashira, M. Oshima, T. Ohnishi, M. Lippmaa, K. Ono, M. Kawasaki, and H. Koinuma, High-resolution synchrotron-radiation photoemission characterization for atomically-controlled $SrTiO_3$(001) substrate surfaces subjected to various surface treatments, J. Appl. Phys. **96**, 7183 (2004).

[26] A. Biswas, C. H. Yang, R. Ramesh, and Y. H. Jeong, Atomically flat single terminated oxide substrate surfaces, Prog. Surf. Sci. **92**, 117 (2017).

[27] V. Stevanović, S. Lany, D. S. Ginley, W. Tumas, and A. Zunger, Assessing capability of semiconductors to split water using ionization potentials and electron affinities only, Phys. Chem. Chem. Phys. **8**, 3706 (2014).

[28] K. Y. Tsou and E. B. Hensley, Electron affinities of the alkaline earth chalcogenides, J. Appl. Phys. **45**, 47 (1974).

[29] R. Sachs, Z. Lin, and J. Shi, Ferroelectric-like $SrTiO_3$ surface dipoles probed by graphene, Sci. Rep. **4**, 1 (2015).

[30] Z. Ren, A. A. Taskin, S. Sasaki, K. Segawa, and Y. Ando, Observations of two-dimensional quantum oscillations and ambipolar transport in the topological insulator Bi_2Se_3 achieved by Cd doping, Phys. Rev. B - Condens. Matter Mater. Phys. **84**, 075316 (2011).

[31] J. Tian, C. Chang, H. Cao, K. He, X. Ma, Q. Xue, and Y. P. Chen, Quantum and classical magnetoresistance in ambipolar topological insulator transistors with gate- tunable bulk and surface conduction, Sci. Rep. **4**, 16 (2014).

[32] A. A. Taskin, S. Sasaki, K. Segawa, and Y. Ando, Manifestation of Topological Protection in Transport Properties of Epitaxial Bi_2Se_3 Thin Films, Phys. Rev. Lett. **109**, 066803 (2012).

[33] N. W. Ashcroft and N. D. Mermin, *Solid State Physics* (Harcourt College Publishers, Fort Worth, 1976).

[34] H. Zhang, C.-X. Liu, X.-L. Qi, X. Dai, Z. Fang, and S.-C. Zhang, Topological insulators in Bi_2Se_3, Bi_2Te_3 and Sb_2Te_3 with a single dirac cone on the surface, Nat. Phys. **5**, 438 (2009).

[35] Y. R. Sapkota, A. Alkabsh, A. Walber, H. Samassekou, and D. Mazumdar, Optical evidence for blue shift in topological insulator bismuth selenide in the few-layer limit, Appl. Phys. Lett. **110**, 181901 (2017).

[36] N. J. G. Couto, B. Sacépé, and A. F. Morpurgo, Transport through Graphene on $SrTiO_3$, Phys. Rev. Lett. **107**, 225501 (2011).

[37] S. Hikami, A. I. Larkin, and Y. Nagaoka, Spin-orbit interaction and magnetoresistance in the two dimensional random system, Prog. Theor. Phys. **63**, 707 (1980).

[38] A. A. Taskin, Z. Ren, S. Sasaki, K. Segawa, and Y. Ando, Observation of Dirac Holes and Electrons in a Topological Insulator.

[39] J. Andzane, G. Kunakova, S. Charpentier, V. Hrkac, L. Kienle, M. Baitimirova, T. Bauch, F. Lombardi, and D. Erts, Catalyst-free vapour-solid technique for deposition of Bi_2Te_3 and Bi_2Se_3 nanowires/nanobelts with topological insulator properties, Nanoscale **7**, 15935 (2015).

[40] F. C. Marques and J. J. Jasieniak, Ionization potential and electron attenuation length of titanium dioxide deposited by atomic layer deposition determined by photoelectron spectroscopy in air, Appl. Surf. Sci. **422**, 504 (2017).